Observation of a Dynamical Quantum Phase Transition by a Superconducting Qubit Simulation

Xue-Yi Guo,[1,2] Chao Yang,[1,2] Yu Zeng,[1,2] Yi Peng,[1,2] He-Kang Li,[1,2] Hui Deng,[3] Yi-Rong Jin,[1,4] Shu Chen,[1,2,*] Dongning Zheng,[1,2,4,5,†] and Heng Fan[1,2,4,5,‡]

[1] *Beijing National Laboratory for Condensed Matter Physics, Institute of Physics, Chinese Academy of Sciences, Beijing 100190, China*

[2] *School of Physical Sciences, UCAS, Beijing 100190, China*

[3] *Synergetic Innovation Centre in Quantum Information and Quantum Physics, USTC, Hefei 230026, China*

[4] *CAS Center for Excellence in Topological Quantum Computation, UCAS, Beijing 100190, China*

[5] *Songshan Lake Materials Laboratory, Dongguan 523808, China*

(Received 26 July 2018; revised manuscript received 28 December 2018; published 24 April 2019)

A dynamical quantum phase transition can occur during time evolution of sudden quenched quantum systems across a phase transition. It corresponds to the nonanalytic behavior at a critical time of the rate function of the quantum-state return amplitude, analogous to nonanalyticity of the free-energy density at the critical temperature in macroscopic systems. A variety of many-body systems can be represented in momentum space as a spin-1/2 state evolving on the Bloch sphere, where each momentum mode is decoupled and thus can be simulated independently by a single qubit. Here, we report the observation of a dynamical quantum phase transition in a superconducting qubit simulation of the quantum-quench dynamics of many-body systems. We take the Ising model with a transverse field as an example for demonstration. In our experiment, the spin state, which is initially polarized longitudinally, evolves based on a Hamiltonian with adjustable parameters depending on the momentum and strength of the transverse magnetic field. The time-evolving quantum state is read out by state tomography. Evidence of dynamical quantum phase transitions, such as paths of time-evolution states on the Bloch sphere, nonanalytic behavior of the dynamical free energy, and the emergence of Skyrmion lattice in momentum-time space, is observed. The experimental data agrees well with theoretical and numerical calculations. The experiment demonstrates explicitly the topological invariant, both topologically trivial and nontrivial, for dynamical quantum phase transitions. Our results show that the quantum phase transitions of this class of many-body system can be simulated successfully with a single qubit by varying certain control parameters over the corresponding momentum range.

DOI: 10.1103/PhysRevApplied.11.044080

I. INTRODUCTION

Quantum simulation can provide insight into quantum and topological phases of matter, the role of entanglement, and quantum dynamics [1–19]. It also constitutes one of the basic building blocks of quantum information processing. Systems of high dimension or many-body systems can be simulated by the quantum processors with many coherently coupled qubits [3,4]. By increasing the number of qubits, the simulation may outperform classical machines, and demonstrate quantum advantage. On the other hand, a variety of many-body systems with a large number of spin-1/2 states can be studied in momentum space by a two-band model with decoupled momentum modes, which is equivalent to a single spin-1/2 state evolving on the Bloch sphere for each mode. This fact also provides a route for quantum simulation with one qubit and variables sweeping over momentum space, by means of coordinate momentum transformation.

In this paper, we emulate the dynamical quantum phase transition (DQPT) of the many-body systems by a single superconducting qubit. The DQPT is a phenomenon occurring in evolving quantum states [20–22] for isolated quantum systems far from equilibrium [23]. It is characterized by the nonanalyticity in dynamical free-energy density at a critical time $t = t_c$, which is analogous to traditional phase transitions occurring at critical temperature. The DQPT is intimately related to quantum phase transitions in many-body systems [20–22,24–36].

*schen@iphy.ac.cn
†dzheng@iphy.ac.cn
‡hfan@iphy.ac.cn

Recently, experimental explorations of DQPT have been performed in ion-trap systems [3,5] and cold-atom systems [4,6] with dozens of individual addressable qubits or a cloud of fermionic atoms. Our experiment follows the DQPT-simulation approach by emulating a corresponding two-band model separately for each momentum mode with a single qubit. By ranging over the Brillouin zone of momentum space, the results are equivalent to that of simulating many-body systems in space. The finite-size effect can be observed for a finite number of momenta implemented experimentally. Our experimental system consists of superconducting Xmon qubits, which is one of the most promising platforms for quantum simulation and quantum computation [37–41]. We provide concrete evidence that the DQPT is successfully simulated. In particular, we demonstrate experimentally the topological invariant in DQPT, which was studied recently in Refs. [24,33], and obtain quantitatively the dynamical free energy and Skyrmion lattice.

II. MODEL AND SCHEME FOR SIMULATION

We begin with a two-band model with the Hamiltonian written in momentum space as

$$H = \sum_k \Psi_k^\dagger h(k) \Psi_k, \tag{1}$$

where Ψ_k denotes a spinor, which is a two-dimensional column vector formed by the fermion operators. The "first quantized" Hamiltonian $h(k)$ for the k momentum mode takes the form

$$h(k) = d_0(k) + \mathbf{d}(k) \cdot \boldsymbol{\sigma}, \tag{2}$$

where $\boldsymbol{\sigma} = (\sigma_x, \sigma_y, \sigma_z)$ is a vector of Pauli matrices and k is in the Brillouin zone. This model can describe a variety of physically different many-body systems [42–45], see the Appendix for details.

To study the quench dynamics, we first prepare the system in the ground state of the initial Hamiltonian $h_i(k)$, i.e., $\rho_i(k) = |\phi_i(k)\rangle\langle\phi_i(k)| = \frac{1}{2}[1 - \hat{\mathbf{d}}_i(k) \cdot \sigma]$. Then with a sudden quench to the final Hamiltonian $h_f(k)$, which determines $\mathbf{d}_f(k)$ by Eq. (2), the state evolves as

$$\rho(k,t) = |\phi(k,t)\rangle\langle\phi(k,t)| = \frac{1}{2}\left[1 - \hat{\mathbf{d}}(k,t) \cdot \sigma\right], \tag{3}$$

where

$$\hat{\mathbf{d}}(k,t) \cdot \boldsymbol{\sigma} = e^{-it\mathbf{d}_f(k)\cdot\boldsymbol{\sigma}} \left[\hat{\mathbf{d}}_i(k) \cdot \boldsymbol{\sigma}\right] e^{it\mathbf{d}_f(k)\cdot\boldsymbol{\sigma}}. \tag{4}$$

This is simply the spin precession on the Bloch sphere, that is, $\hat{\mathbf{d}}_i(k)$ rotating around $\hat{\mathbf{d}}_f(k)$ with period $\pi/|\mathbf{d}_f(k)|$.

Now we introduce the rate function of the dynamical free energy,

$$f(t) = -\frac{1}{N}\sum_k \log |\langle\phi_i(k)| e^{-ith_f(k)} |\phi_i(k)\rangle|^2. \tag{5}$$

The nonanalytic behavior of $f(t)$ corresponds to DQPT, which is associated with zeros of $\langle\phi_i(k)| e^{-ith_f(k)} |\phi_i(k)\rangle$ for at least one critical momentum k^* at critical time t_c. From the spin-precession picture, it is clear that spin vector $\mathbf{d}_i(k^*)$ is perpendicular to the rotation axis $\mathbf{d}_f(k^*)$, where $\mathbf{d}_i(k^*) \neq 0$, $\mathbf{d}_f(k^*) \neq 0$, and t_c repeats with period $\pi/|\mathbf{d}_f(k^*)|$.

In this paper, without loss of generality, we investigate experimentally the DQPT of the Ising model with a transverse field, but the approach is applicable to other similar phenomena of many-body systems. The Hamiltonian of the transverse-field Ising model is

$$H_{\text{Ising}} = -\sum_{i=1}^{N} \left(\sigma_i^x \sigma_{i+1}^x + g\sigma_i^z\right), \tag{6}$$

where g is the strength of the field in the Z direction, and the periodic boundary condition is assumed. There are two phases for this model, the ferromagnetic phase for $g < 1$, and the paramagnetic phase for $g > 1$; the phase-transition critical point is $g_c = 1$. It is proved that DQPT occurs if and only if the initial Hamiltonian with a g_i field and the quenching Hamiltonian with a g_f field belong to different phases [20].

The scheme for simulating DQPT in experiment is as follows. We first prepare the initial qubit state $|\phi_i(k)\rangle$ determined by parameter g_i for each mode k. By the sudden quench, state $|\phi_i(k)\rangle$ evolves as $|\phi(k,t)\rangle$ according to the Hamiltonian, $h_f(k) = (g_f - \cos k)\sigma^y + \sin k\sigma^x$, which depends on parameter g_f, i.e., the spin vector $\hat{\mathbf{d}}_i(k)$ rotates around axis $\hat{\mathbf{d}}_f(k)$ on the Bloch sphere, see the Appendix for details. The time-evolution state $|\phi(k,t)\rangle$ is read out experimentally by state tomography. By ranging over the Brillouin zone of momentum space for each mode k, we can obtain the rate function in Eq. (5). The occurrence of DQPT can be observed when the rotation path of $|\phi(k,t)\rangle$ is a great circle on the Bloch sphere for mode $k = k^*$. In this case, $|\phi(k^*,t)\rangle$ is orthogonal to the initial state at time t_c, $\langle\phi_i(k^*)|\phi(k^*,t_c)\rangle = 0$, resulting in a nonanalytic point of the rate function. For the full regime of k in the Brillouin zone, the time evolutions of states $|\phi(k,t)\rangle$ cover the full Bloch sphere when there exists DQPT, otherwise only less than one half of the Bloch sphere is covered, as recently pointed out by our co-authors [24,33]. This phenomenon is observed as one of the signatures in identifying the occurrence of DQPT. It is actually a direct observation of the topological invariant.

III. EXPERIMENTAL SETUP

In the experiment we use a single qubit to simulate the dynamics of the model. Figure 1 is the microscopic photograph of the superconducting Xmon qubit chip [37], the external circuitries and qubit parameters. In experiment, the Xmon qubit is biased at its maximum frequency of 6.203 GHz—also known as the sweet spot. The measured anharmonicity is about -236 MHz, the measured energy relaxation time T_1 about 8.3 μs, dephasing time T_{2*} about 6.8 μs, and spin-echo dephasing time T_{2se} about 11.7 μs. The readout cavity frequency is about 6.793 GHz, which falls in the dispersive coupling regime. The frequency dispersive shift of the readout cavity is $\kappa/2\pi = -0.697$ MHz.

The energy gap of the qubit can be adjusted by an external flux bias. The Xmon qubit is capacitively coupled to a $\lambda/4$ coplanar waveguide (CPW) resonator that is coupled to a CPW transmission line. In this device, the qubit state is read out by the dispersive method via the $\lambda/4$ resonator. The optical micrograph of this sample is shown in Fig. 1(a). Details of chip fabrication and the circuitry are presented in the Appendix.

IV. TIME-EVOLUTION PATHS ON THE BLOCH SPHERE FOR DQPT

Following our experimental scheme, we first prepare the initial state as the ground state of the Hamiltonian $h_i(k)$ for a fixed mode k, then suddenly quench the system to the final Hamiltonian $h_f(k)$. For convenience, we actually always prepare the initial state as $|\phi_i\rangle = (|0\rangle + |1\rangle)/\sqrt{2}$, consequently the quenched Hamiltonian is changed accordingly. This is because we can perform a rotation to both Hamiltonians, $h_i(k)$ and $h_f(k)$, without changing the DQPT results.

The quenched quantum state is read out at a sequence of time points to obtain the time-dependent density matrix $\rho(k,t)$. For a full rotation period, we can obtain a circular evolution path of the state on the Bloch sphere. The same procedure repeats by changing momentum k in the Brillouin zone.

In the experiment, we let $g_i = 0.2$, which is in the ferromagnetic phase regime. The system is suddenly quenched to the final Hamiltonian $h_f(k)$. Here two different strengths of the field are chosen, $g_f = 0.5$ and $g_f = 1.5$, corresponding to the ferromagnetic and paramagnetic phases, respectively.

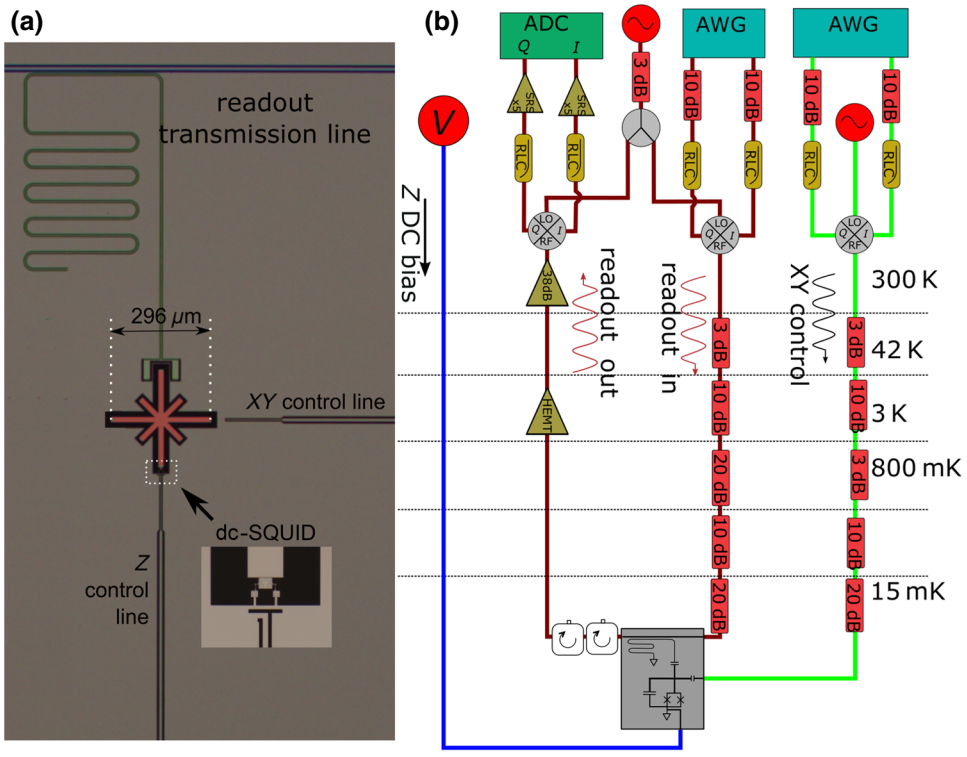

FIG. 1. Photography of qubit chip and external circuitries. (a) Microscopic photography of our Xmon qubit chip. The red part is the Xmon qubit. Its frequency can be adjusted by applying dc current through its Z control line. The transmission line coupled to the readout cavity is to measure the qubit state. Basic information of the qubit is listed in the table. The experiment data of the energy relaxation time T_1, dephasing time T_{2*} and spin-echo dephasing time T_{2se} are also shown. (b) Sketch of our experiment circuit setup, the blue part is for Z bias, the green part is for XY control, and the brown part is for readout. (c) Qubit parameters are presented in the table.

(c)

$f_{01}^{\max}$	$f_{12}^{\max} - f_{01}^{\max}$	T_1	T_2^*	T_2^{se}	$f_{\text{readoutcavity}}$
6.203 GHz	-236 MHz	8.3 μs	6.8 μs	11.7 μs	6.793 GHz

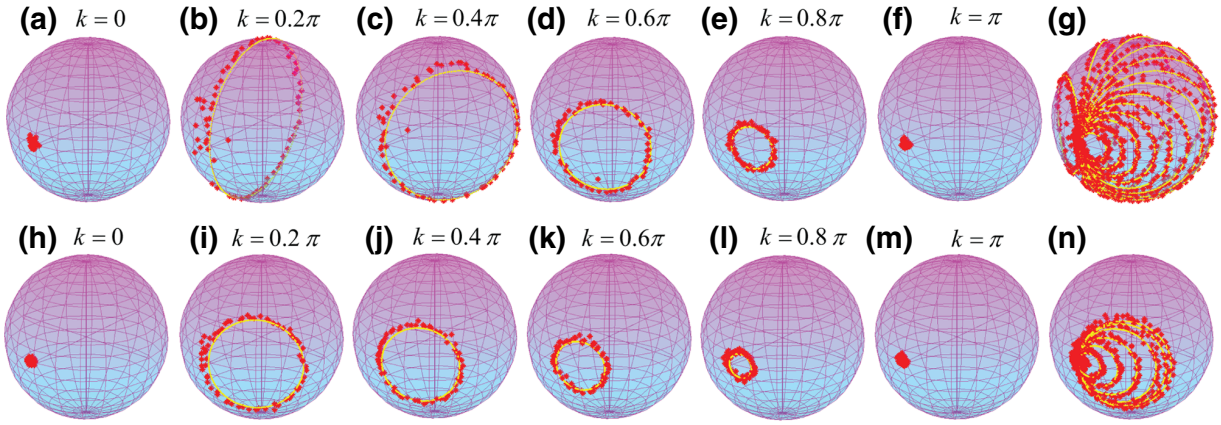

FIG. 2. Evolution of states on the Bloch sphere. The state evolves depending on a fixed momentum. Data of the evolving path are presented on the Bloch sphere. Here $g_i = 0.2$ is fixed, cases with $g_f = 1.5$ are presented in (a)–(g) in the upper panel, cases of $g_f = 0.5$ are presented in (h)–(n) in the lower panel. The momenta are chosen to be $k = 0, 0.2\pi, 0.4\pi, 0.6\pi, 0.8\pi, \pi$, presented, respectively, on up-down pairs of subfigures: (a),(h); (b),(i); (c),(j); (d),(k); (e),(l); (f),(m). Data for two different cases are summarized together in (g) for $g_f = 1.5$, and (n) for $g_f = 1.5$, respectively. We can find that the whole Bloch sphere in (g) is covered, in contrast in (n), only a partial region of the Bloch sphere is covered. We emphasize that the initial state is always prepared on the equator of the Bloch sphere in the X axis.

The qubit is first rotated about the Y axis by a $\pi/2$ microwave pulse to the superposed state $|\phi_i\rangle = (|0\rangle + |1\rangle)/\sqrt{2}$. For a fixed k, a unitary operation based on the final Hamiltonian is applied to the initial state $|\phi_i\rangle$ as the quantum-quench procedure. We then sweep mode k in the Brillouin zone from 0 to 2π with step length $2\pi/30$.

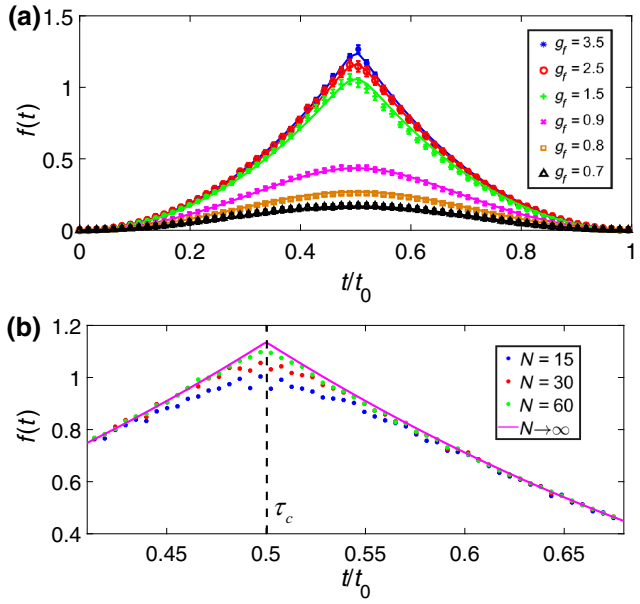

FIG. 3. Dynamical free energy. (a) Dynamical free energies for different g_f are presented, while $g_i = 0.2$ is fixed. We take 70 time points for each period. The error bar represents the deviation of the average value of 5000 single-shot measurements from the fitting value for the evolution path of 70 points on the Bloch sphere, see the Appendix for details. (b) The dynamical free energies near the critical time τ_c for a different number of momenta implemented in experiment are given, corresponding to different sizes. The exact results for $N \to \infty$ are presented as the solid line. Here we take $g_i = 0.2$ and $g_f = 1.5$.

For each value of k, the state is rotated for two cycles on the Bloch sphere, representing time evolution for two periods. The rotation axis is determined by the quench Hamiltonian $h_f(k)$. The path of the state time evolution is presented in Fig. 2, where only one cycle of data is presented. In the figure, each dot represents the evolving state at a fixed time point read out experimentally by state tomography. For example, Figs. 2(a) and 2(h) represent $k = 0$ for different quenched Hamiltonians. We can find that the initial state always stays at its original position, because the rotation axis is the X direction determined by the corresponding Hamiltonian.

Figures 2(a)–2(g), seven subfigures in the upper panel, represent the system is suddenly quenched to $g_f = 1.5$, and the state evolutions on the Bloch sphere for $k = 0$, 0.2π, 0.4π, 0.6π, 0.8π, π are presented in the first six subfigures, respectively. All data for this case are presented together in Fig. 2(g), where those k modes are for $k \in [0, \pi]$ constituting a half region in the Brillouin zone. For each mode k, the state starts from $|\phi_i\rangle$ in the original position and evolves like a circle on the Bloch sphere. In each cycle of time period, we take 70 time points for state-tomography readout. The experimental data are presented as dots on the Bloch sphere, where each dot represents the average value of 5000 single-shot measurement results. Each step of time evolution lasts 15 ns. Then one circle of period takes 1.05 μs, two circles are also performed experimentally, they are within the coherence time. We also take a normalization, $|\langle|\phi(k,t)|\phi(k,t)\rangle|^2 = 1$, at each time point, implying pure states are assumed for time evolution, $\mathrm{Tr}\rho^2(k,t) = 1$. We take a total of 30 different momenta k

in the Brillouin zone in experiment, the evolution paths are given in Fig. 2(g).

Figures 2(h)–2(n), seven subfigures in the lower panel, represent the case that the system is suddenly quenched to $g_f = 0.5$. Similar conventions are used as those in the upper panel.

The occurrence of DQPT can be directly observed in Fig. 2. It is obvious that in the upper panel of the figure, Figs. 2(a)–2(g), the full Bloch sphere is covered by the time-evolution paths of the states shown explicitly in Fig. 2(g). This case is that $g_f = 1.5$ and $g_i = 0.2$ are located in two different phases, so DQPT happens. Since the full Bloch sphere is covered, it is apparent that there exists a k^*, the path of the evolving state is a great circle resulting in that state $|\phi_i^{\perp}\rangle = (|0\rangle - |1\rangle)/\sqrt{2}$, located in the opposite direction of the X axis on the Bloch sphere, can be reached at a critical time t_c, shown in Fig. 2(b). The orthogonality leads to zero for overlap between the evolving state $|\phi_i^{\perp}\rangle$ with the initial state $|\phi_i\rangle$, leading to nonanalyticity for the logarithm in the rate function (5). These results demonstrate the occurrence of DQPT at a critical time t_c. In contrast, when $g_i = 0.2$ is quenched to $g_f = 0.5$ but without going across the critical point $g_c = 1$, we can observe in Figs. 2(h)–2(n) that only less than one half of the Bloch sphere is covered for k in the Brillouin zone, as summarized in Fig. 2(n). Then no DQPT can happen.

V. THE RATE FUNCTION, FINITE-SIZE EFFECT, AND THE SKYRMION LATTICE

Quantitatively, we can obtain the evolution of dynamical free energy defined in Eq. (5). Figure 3(a) presents the time-dependent rate functions for different g_f, all with initial parameter $g_i = 0.2$. The experimental data are shown as dots, the theoretical results are presented as lines. We can find that the rate functions $f(t)$ have sharp peaks at the critical time t_c for $g_f = 3.5, 2.5, 1.5$, which leads to discontinuity for derivative of $f(t)$ at t_c. This phenomenon corresponds to the DQPT. In comparison, it is obvious that the rate functions for $g_f = 0.9, 0.8, 0.7$ are different from cases when $g_f > 1$. The curves are much more smooth and no sharp peak appears, so no discontinuity is expected for derivative of the rate functions. Thus no DQPT happens. The results agree well with theoretical calculations.

Figure 3(b) shows the results of a different number N of modes for k, corresponding to size N of the Ising model. So experiments are performed for N equally separated momenta for $k \in [0, 2\pi]$. Here $g_i = 0.2$ and $g_f = 1.5$ are fixed. It can be found that if t is far away from t_c, the dynamical free energy $f(t)$ is quite close to the theoretic value (pink curve) of $N \to \infty$. Near the critical time t_c, $f(t)$ is nearly smooth if the size is small, demonstrating the finite-size effect. As N increases, it approaches the

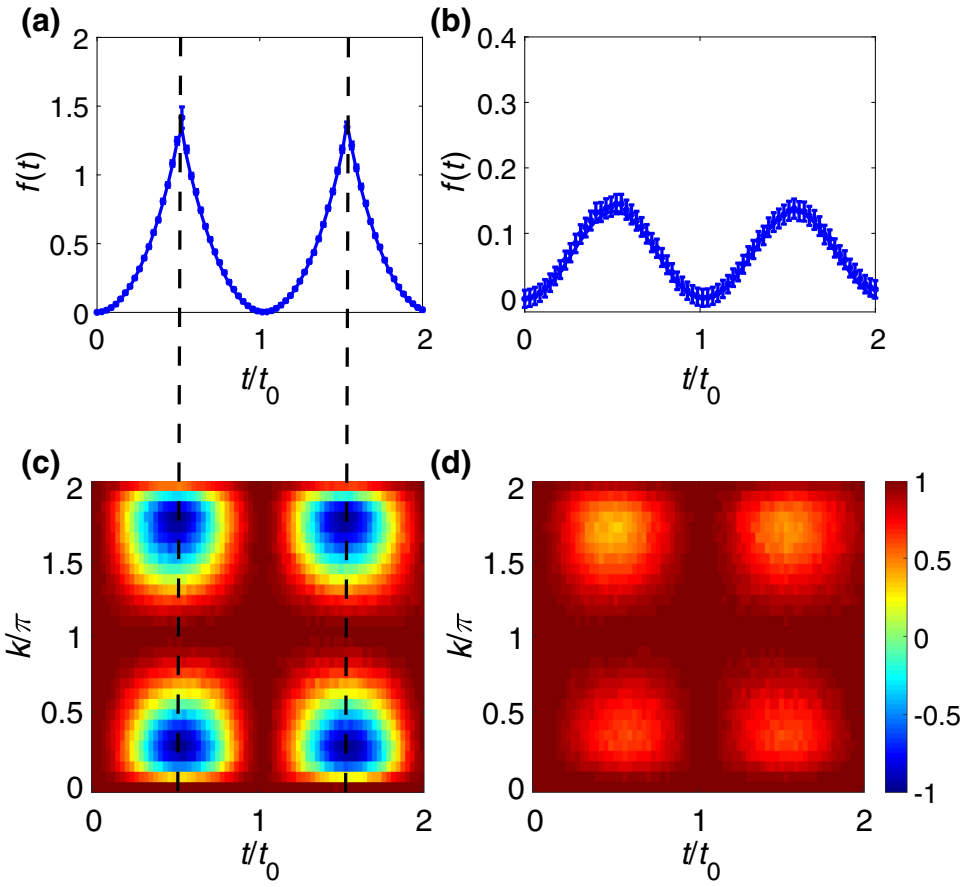

FIG. 4. Skyrmion and DQPT. (a),(b) Dynamical free energies for $g_f = 1.5$ and $g_f = 0.5$, both with $g_i = 0$, respectively. The number of momenta is $N = 30$. For each momentum mode k, states at $2 \times 70 = 140$ time points are read out. The error bar is the deviation of the average value from the fitting value, see the Appendix for details. (c),(d) Expectation values of the initial spin operator about the evolving state $|\phi(k,t)\rangle$. The Skyrmion is shown obviously in (c), while no Skyrmion appears in (d).

theoretical value for $N \to \infty$ and demonstrates nonanalytic behavior.

Figure 4 shows the emergence of a Skyrmion lattice in momentum-time space for DQPT. We define the expectation value as $\langle \hat{\mathbf{d}}(k,t)\rangle = \langle \phi(k,t)|\hat{\mathbf{d}}_i|\phi(k,t)\rangle$, see also the Appendix. We consider two different cases, $g_f = 1.5$ in Fig. 4(c) and $g_f = 0.5$ in Fig. 4(d), both start from the initial condition $g_i = 0$. The rate functions are presented, respectively, in Figs. 4(a) and 4(b) for comparison. We find that when $g_i = 0$ and $g_f = 1.5$ lie in different phases, the emergence of the Skyrmion lattice in momentum-time space can be seen obviously in Fig. 4(c), which indicates the nontrivial dynamical Chern number implying the occurrence of DQPT. The time coordinates of the center of Skyrmion is just the critical time t_c. While if $g_i = 0$ and $g_f = 0.5$ lie in the same phase, the configuration of the Skyrmion lattice does not appear as shown in Fig. 4(d), the corresponding dynamical Chern number is trivial. There is no DQPT as shown Fig. 4(b).

VI. CONCLUSION AND DISCUSSION

In summary, we simulate successfully the two-band model of DQPT for the transverse-field Ising model by a single superconducting qubit. The DQPT is shown by state-evolution paths on the Bloch sphere, the dynamical free energy, and the Skyrmion lattice. The critical time of DQPT is quantitatively identified. This approach is applicable in investigating various physical phenomena of the class of free fermionic many-body systems. A similar experimental scheme can be applied to simulate temporal topological phenomena by demonstrating that a single qubit is driven by two elliptically polarized periodic waves [45].

In our scheme, phenomena of many-body systems are simulated by a single qubit at the expense of repeating experiments by ranging over the momentum space. On the other hand, besides the two-level system, it is known that the superconducting Josephson junction can have controllable multiple energy levels. Then, this platform is promising for more simulating applications, such as the *PT*-symmetric physics, geometric quantum logic gates for quantum computation. Also, the superconducting qubit or multilevel system can be coupled to bosonic modes by a resonator or cavity, simulations such as spin-boson phenomena, quantum random walks and quantum statistical models are expected. So, our results pave the way for more applications of the superconducting quantum platform.

ACKNOWLEDGMENTS

The first two authors, X.Y.G. and C.Y., contributed equally to this work. We thank Wuxin Liu and Haohua Wang of Zhejiang University for technical support. We thank Ling-An Wu for carefully reading our manuscript to improve our presentation. This work is supported by National Key Research and Development Program of China (Grants No. 2016YFA0302104, No. 2016YFA0300600, No. 2014CB921401, No. 2017YFA0304300), National Natural Science Foundation of China (Grants No. 11425419, No. 11404386, No. 11674376, No. 11774406), and Strategic Priority Research Program of Chinese Academy of Sciences (Grant No. XDB28000000).

APPENDIX A: QUBIT DEVICE AND EXTERNAL CIRCUITRIES

The sample is fabricated using a process involving electron-beam-lithography (EBL) and double-angle evaporation. In brief, a 100-nm-thick Al layer is firstly deposited on a 10×10 mm sapphire substrate by means of electron-beam evaporation, followed by EBL and wet etching to produce large structures such as microwave coplanar-waveguide resonators and transmission lines, capacitors of the Xmon qubit, and electric leads. The EBL resist used is ZEP520 and wet-etching process is carried out using Aluminum Etchant Type A. In the next step, the Josephson junctions of qubits are fabricated using the double-angle evaporation process. In this step, the undercut structure is created using a PMMA-MMA double layer EBL resist following a process similar to that reported in Ref. [37]. During the evaporation, the bottom electrode was about 30 nm thick while the top electrode is about 100 nm thick with intermediate oxidation.

In the measurements, the sample is mounted in an aluminum alloy sample box, which is fixed on the mixing chamber stage of a dilution refrigerator. The temperature of the mixing chamber is below 15 mK during measurements. The readout input microwave lines and qubit *XY* control lines are heavily attenuated. Lines for qubit dc bias control are filtered using filters (RLC ELECTRONICS F-10-200-R) that function as a combination of low-pass filter and copper powder filter. The microwave output signal from the transmission line is amplified (approximately equal to 39 dB) by a cryogenic HEMT amplifier mounted at the 4-K stage and a room-temperature amplifier (approximately equal to 38 dB) before being measured by a home-built heterodyne acquisition system shown in Fig. 1(b) in the main text.

APPENDIX B: PHYSICAL DESCRIPTION OF THE SUPERCONDUCTING QUBIT

In the past decades, there has been a great progress in the field of superconducting qubits. The main aims are to achieve better control and longer coherent time for qubit or qubits. As a result, many types of superconducting qubits have been developed, each of which has its own advantages and limits. There are three main categories of the quantum superconducting qubit working in different regimes according the ratio of the Josephson energy E_J to the charging energy E_C [46–49]: (1) charge qubit

with $E_J/E_C \sim 0.1$; (2) flux qubit with $E_J/E_C \sim 50$; and (3) phase qubit $E_J/E_C \sim 10^6$. By adding a large capacitor C_S parallel to the superconducting quantum interference device (SQUID) and thus shunting the later [cf. Fig. 5(a)], the transmon qubit works in the parameter regime of E_J/E_C being the order of several tens or several hundreds. It gains the advantage of exponentially suppressing the sensitivity to the charge noise at the expense of polynomial reduction of the anharmonicity [38,46–49]. Notice that anharmonicity describes the variation of the energy-level spacing, which ensures the possibility of addressing the lowest energy levels of the platform. The Hamiltonian of an isolated transmon qubit is

$$\hat{H}_0 = 4E_C\hat{n}^2 - E_J\cos\hat{\phi}, \tag{B1}$$

where $\hat{n}$ is the operator corresponding to the number of Cooper pairs tunneled through the Josephson junctions and $\hat{\phi}$ denotes the gauge-invariant phase-difference operator across the Josephson junctions. They are mutually conjugate and satisfy the commutation relation $[\hat{\phi},\hat{n}] = i$. The charging energy $E_C = e^2/2C_\Sigma$ depends on the total capacitance $C_\Sigma = C_S + C_g + C_J$ of the shunt capacitor C_S, gate capacitor C_g and the Josephson-junction capacitance C_J. The Josephson energy $E_J = \hbar I_C/2e$ is determined by the critical current of the dc SQUID, which is modulated by the external magnetic flux. In the transmon regime, C_S is very large such that $20 \lesssim E_J/E_C \lesssim 100$, its ℓth eigenenergy level should be [38,46–49]

$$E_\ell \simeq -E_J + \sqrt{8E_JE_C}(\ell + 1/2) - \frac{1}{2}E_C[\ell(\ell+1) + 1/2]. \tag{B2}$$

The anharmonicity is big enough for the addressability of the two lowest energy levels and thus constitutes a qubit

$$\hat{H}_0 = \frac{1}{2}\hbar\omega\hat{\sigma}_z, \tag{B3}$$

with $\omega = 2(\sqrt{8E_JE_C} - E_C)/\hbar$ and $\hat{\sigma}_z = |e\rangle\langle e| - |g\rangle\langle g|$. Here $|g\rangle$ is the ground state of the transmon while $|e\rangle$ is its first excited eigenstate.

The quantum platform we employ is a superconducting Xmon qubit, which is designed on the basis of coplanar transmon. Essentially it is equivalent to a grounded transmon, see Fig. 5. Embedded in an uninterrupted ground plane, the Xmon qubit can prolong the coherent time by further employing a coplanar waveguide made with high-quality material. Better connectivity can be accomplished via a cross-shaped capacitor [37,46–49]. The driving microwave applied as shown in Fig. 5(b) is the following:

$$V_g = V\cos(\omega t + \phi_0). \tag{B4}$$

The frequency of the microwave is chosen to match the resonant frequency of the isolated qubit in Eq. (B3). As a result, the Hamiltonian of the Xmon is

$$\hat{H} = 4E_C\hat{n}^2 + \frac{V_gC_g\hat{n}e}{C_\Sigma} - E_J\cos\hat{\phi}. \tag{B5}$$

The two-level qubit Hamiltonian via truncating all the higher-energy levels is thus

$$\hat{H} = \frac{1}{2}\hbar\left(\omega + \omega_\Phi\right)\hat{\sigma}_z + \frac{AC_ge}{C_\Sigma}\cos(\omega t + \phi_0)\hat{\sigma}_x, \tag{B6}$$

where ω_Φ is the energy-level shift caused by the external magnetic flux $\Phi_{\rm ext}$ controlled by varying $I_{\rm ext}$. Moving to the interaction picture with respect to $\hat{H}_0$, we have

$$\hat{H}_r = \hbar\omega_\Phi\hat{\sigma}_z + \frac{AC_ge}{C_\Sigma}\left(\cos\phi_0\hat{\sigma}_x + \sin\phi_0\hat{\sigma}_y\right). \tag{B7}$$

By varying the amplitude A and phase ϕ_0 of the driving voltage V_g, which is applied through the gate capacitor C_g, we would have full control of the rotations of the qubit along the X as well as the Y direction. The Z-direction control is exerted via the change control current $I_{\rm ext}$, which adjusts the external magnetic flux $\Phi_{\rm ext}$ thrusting through the SQUID loop.

APPENDIX C: MANY-BODY SYSTEMS AND THE TWO-BAND MODEL

The Hamiltonian of a two-band model is written as

$$H = \sum_k \Psi_k^\dagger h(k)\Psi_k, \tag{C1}$$

where Ψ_k denotes a spinor, $h(k)$ takes the form

$$h(k) = d_0(k) + \mathbf{d}(k)\cdot\boldsymbol{\sigma}, \tag{C2}$$

where $\boldsymbol{\sigma} = (\sigma_x, \sigma_y, \sigma_z)$ is a vector of Pauli matrices, as already presented in the main text. This model can describe

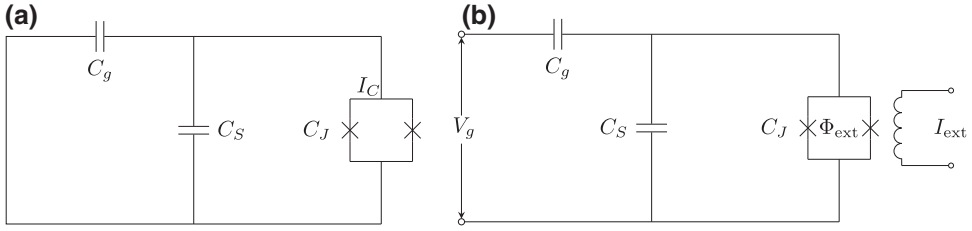

FIG. 5. Equivalent circuits of (a) the isolated transmon circuit and (b) its Xmon variety with control. (a) Isolated transmon circuit, (b) Xmon circuit with control.

a variety of physically different many-body systems. For examples, the Su-Schrieffer-Heeger (SSH) model [42] describes the simplest one-dimensional topological insulator. We have that $\Psi_k^\dagger = (c_{kA}^\dagger, c_{kB}^\dagger)$ with A and B referring two sublattices, $\mathbf{d}(k) = [(t+\delta t) + (t-\delta t)\cos k, (t-\delta t)\sin k, 0)]$, with $(t \pm \delta t)$ being the hopping amplitudes in the unit cell and between the adjacent cells, respectively. Another example is the p-wave Kitaev chain [43], which describes a one-dimensional topological superconductor. For this case, we have that $\Psi_k^\dagger = (c_k^\dagger, c_{-k})$ and $\mathbf{d}(k) = [0, \Delta \sin k, (-\mu/2 - t\cos k)]$, where Δ denotes the pairing potential, μ the chemistry potential, t the hopping amplitude. When $t = \Delta$, it corresponds to the transverse-field Ising model [44] after mapping to the free fermions by Jordan-Wigner transformation. Here, we have $\mathbf{d}(k) = [0, \sin k, (g - \cos k)]$. The details are as follows.

The SSH model is the simplest two-band model describing polyacetylene, which is a one-dimensional topological insulator. The Hamiltonian reads

$$H_{\mathrm{SSH}} = \sum_l (t+\delta t) c_{A,l}^\dagger c_{B,l} + (t-\delta t) c_{A,l+1}^\dagger c_{B,l} + \mathrm{h.c.} \tag{C3}$$

A and B refer to two sublattices. The hopping amplitude in the unit cell is $t + \delta t$ while that between adjacent unit cell is $t - \delta t$. Performing the Fourier transformation $c_{kA} = (1/\sqrt{N}) \sum_l e^{-ikl} c_{A,l}$ and $c_{kB} = (1/\sqrt{N}) \sum_l e^{-ikl} c_{B,l}$, where N is the number of sites, we obtain

$$\begin{aligned} H_{\mathrm{SSH}} = &\sum_k (t+\delta t)(c_{kA}^\dagger c_{kB} + \mathrm{h.c.}) \\ &+ (t-\delta t)(e^{ik} c_{kA}^\dagger c_{kB} + \mathrm{h.c.}). \end{aligned} \tag{C4}$$

Introducing the spinor $\Psi_k^\dagger = (c_{kA}^\dagger, c_{kB}^\dagger)$, the Hamiltonian can be written in a compact form,

$$\begin{aligned} H_{\mathrm{SSH}} = &\sum_k \Psi_k^\dagger \{[(t+\delta t) + (t-\delta t)\cos k]\sigma_x \\ &+ (t-\delta t)\sin k \sigma_y\} \Psi_k, \end{aligned} \tag{C5}$$

where $\mathbf{d}(k) = [(t+\delta t) + (t-\delta t)\cos k, (t-\delta t)\sin k, 0)]$ referring to Eq. (C2). The system is topologically nontrivial when $|t+\delta t| < |t-\delta t|$. Otherwise it is topologically trivial.

The p-wave Kitaev chain is a one-dimensional topological superconductor introduced by Kitaev [43]. The Hamiltonian reads

$$\begin{aligned} H_K = &\sum_l -t(c_l^\dagger c_{l+1} + \mathrm{h.c.}) - \Delta(c_l^\dagger c_{l+1}^\dagger + \mathrm{h.c.}) \\ &- \mu\left(c_l^\dagger c_l - \frac{1}{2}\right). \end{aligned} \tag{C6}$$

t is the hopping amplitude; Δ is the p-wave superconductor pairing potential, and μ is the chemical potential. Performing the Fourier transformation $c_k = (1/\sqrt{N}) \sum_l e^{-ikl} c_l$ and introducing the spinor $\Psi_k^\dagger = (c_k^\dagger, c_{-k})$, we obtain

$$H_K = \sum_k \Psi_k^\dagger [\Delta \sin k \sigma_y + (-\mu/2 - t\cos k)\sigma_z] \Psi_k, \tag{C7}$$

where $\mathbf{d}(k) = [0, \Delta \sin k, (-\mu/2 - t\cos k)]$ referring to Eq. (C2). This model is mathematically equivalent to the transverse-field Ising model when $t = \Delta$, and it is topologically nontrivial when $2|t|/|\mu| > 1$.

The transverse-field Ising model is described as

$$H_{\mathrm{Ising}} = -\sum_l \sigma_l^x \sigma_{l+1}^x + g\sigma_l^z. \tag{C8}$$

g is the transverse-field strength. The spin model can be mapped to the free-fermion model by using Jordan-Wigner transformation

$$\sigma_l^z = 1 - 2c_l^\dagger c_l, \quad \sigma_l^x = \prod_{j<l} (1 - 2c_j^\dagger c_j)(c_l + c_l^\dagger). \tag{C9}$$

The Hamiltonian changes to

$$H_{\mathrm{Ising}} = -\sum_l (c_l^\dagger c_{l+1} + c_l^\dagger c_{l+1}^\dagger + \mathrm{h.c.}) + g(1 - 2c_l^\dagger c_l). \tag{C10}$$

Again, by using Fourier transformation and introducing the spinor $\Psi_k^\dagger = (c_k^\dagger, c_{-k})$, we obtain

$$H_{\mathrm{Ising}} = \sum_k \Psi_k^\dagger [\sin k \sigma_y + (g - \cos k)\sigma_z] \Psi_k, \tag{C11}$$

where $\mathbf{d}(k) = [0, \sin k, (g - \cos k)]$, which is used in the main text. It is well known that the model is in ferromagnetic phase when $g < 1$ and in paramagnetic phase when $g > 1$.

For Hamiltonian (C1), see also Eq. (1) in the main text, one can find that each k mode is decoupled, so we can investigate each mode separately. The eigenvalues of $h(k)$ are given by

$$\epsilon_\pm(k) = d_0(k) \pm |\mathbf{d}(k)|. \tag{C12}$$

The corresponding eigenvectors are denoted by $|\phi_\pm(k)\rangle$, or written as density matrices

$$\rho_\pm(k) = |\phi_\pm(k)\rangle\langle\phi_\pm(k)| = \frac{1}{2}\left[1 \pm \hat{\mathbf{d}}(k) \cdot \boldsymbol{\sigma}\right], \tag{C13}$$

where $\hat{\mathbf{d}}(k) = \mathbf{d}(k)/|\mathbf{d}(k)|$ corresponding to a unique vector on the Bloch sphere.

To study the quench dynamics, we first prepare the system in the ground state of the initial Hamiltonian $h_i(k)$, i.e., $\rho_i(k) = |\phi_i(k)\rangle\langle\phi_i(k)| = \frac{1}{2}[1 - \hat{\mathbf{d}}_i(k)\cdot\sigma]$, corresponding to the minus eigenvector in Eq. (C13). Then taking a sudden quench to the final Hamiltonian $h_f(k)$, which determines $\mathbf{d}_f(k)$. The state evolves as $|\phi(k,t)\rangle = e^{-ith_f(k)}|\phi_i(k)\rangle$. A more enlightening picture can be presented as density matrix form,

$$\rho(k,t) = |\phi(k,t)\rangle\langle\phi(k,t)| = \frac{1}{2}[1 - \hat{\mathbf{d}}(k,t)\cdot\sigma], \quad \text{(C14)}$$

where

$$\hat{\mathbf{d}}(k,t)\cdot\boldsymbol{\sigma} = e^{-it\mathbf{d}_f(k)\cdot\boldsymbol{\sigma}}\left[\hat{\mathbf{d}}_i(k)\cdot\boldsymbol{\sigma}\right]e^{it\mathbf{d}_f(k)\cdot\boldsymbol{\sigma}}. \quad \text{(C15)}$$

It is simply the spin precession on the Bloch sphere, that is, $\hat{\mathbf{d}}_i(k)$ rotates around $\hat{\mathbf{d}}_f(k)$ with period $\pi/|\mathbf{d}_f(k)|$.

APPENDIX D: EXPERIMENTAL SCHEME

Experimentally, we prepare the initial state and control its evolution by the corresponding Hamiltonian, see Fig. 6 for the schematic description. The evolving state is read out by state tomography. Our simulation focuses on the case of the transverse-field Ising model, Eqs. (C8), (C11). In general, the initial state should be prepared as $|\phi_i(k)\rangle$ depending on the initial Hamiltonian $h_i(k)$. Without loss of generality, we always prepare the initial state in experiment as

$$|\phi_i\rangle = \frac{1}{\sqrt{2}}(|0\rangle + |1\rangle). \quad \text{(D1)}$$

At the same time, the quenched Hamiltonian should be changed correspondingly. Considering that the prepared initial state $|\phi_i\rangle$ in Eq. (D1) is an eigenvector of σ^x, $\sigma^x = U^\dagger h_i(k)U$, which corresponds to $h_i(k)$ by a unitary transformation U. Then for a quantum quench, the applied Hamiltonian takes the form $U^\dagger h_f(k)U$.

Now, let us show how to realize a qubit rotation in experiment. In the Hamiltonian of a qubit Eq. (B7), the two terms in the parentheses represent a rotation with axis in the X-Y plane. The direction can be adjusted by controlling the parameter ϕ_0 in Eq. (B7), which depends on momentum k. Experimentally as shown in Fig. 6, by controlling φ_k in $A_k\cos(\omega t + \varphi_k)$, we can realize the control of axis direction in the X-Y plane for a rotation. Explicitly in Fig. 2 in the main text, we can find that the rotation axes are in the X-Y plane.

Our simulation scheme can be applied to general two-band models. For example, as shown in Ref. [45], the temporal topological phenomena can be simulated by a qubit subjected to a two-frequency drive. The Hamiltonian takes the form,

$$H_{\text{temp}} = v_1\cos(\omega_1 t + \varphi_1)\sigma^x + v_2\sin(\omega_2 t + \varphi_2)\sigma^y + [m - b_1\cos(\omega_1 t + \varphi_1) - b_2\cos(\omega_2 t + \varphi_2)]\sigma^z, \quad \text{(D2)}$$

where the notations and the implication of this model can be found in Ref. [45]. This Hamiltonian corresponds to Eq. (B7), and can be realized by a superconducting qubit. The rotation axis should be in arbitrary direction. The topological phenomena are described by whether the whole Bloch sphere of the corresponding states are covered or not, which is similar to our experiment.

APPENDIX E: RELATION BETWEEN DYNAMICAL QUANTUM PHASE AND DYNAMICAL CHERN NUMBER

In Ref. [50], it is shown that the Loschmidt amplitude of a two-band system can be written as

$$G(t) = \prod_k[\cos(|\mathbf{d}_f(k)|t) + i\hat{\mathbf{d}}_i(k)\cdot\hat{\mathbf{d}}_f(k)\sin(|\mathbf{d}_f(k)|t)], \quad \text{(E1)}$$

where $\mathbf{d}_i(k)$ and $\mathbf{d}_f(k)$ correspond to the pre and postquench Hamiltonians, respectively. The DQPT occurs when the Loschmidt amplitude reaches zero at a critical time t_c. As we see from Eq. (E1), the existence of zeroes of $G(t)$ requires that there are at least one critical momentum k^* satisfying

$$\hat{\mathbf{d}}_i(k^*)\cdot\hat{\mathbf{d}}_f(k^*) = 0, \quad \text{(E2)}$$

i.e., the vector $\hat{\mathbf{d}}_i(k)$ is perpendicular to $\hat{\mathbf{d}}_f(k)$ at the critical momentum k^*, and the DQPT occurs at

$$t_c = \frac{\pi}{|\mathbf{d}_f(k)|}\left(n + \frac{1}{2}\right), \quad n = 0, 1, 2, \ldots, \quad \text{(E3)}$$

and the Bloch vector satisfies $\hat{\mathbf{d}}(k^*, t_c) = -\hat{\mathbf{d}}_i(k^*)$ [24]. For clarity, we employ the Ising model to elucidate the condition of DQPT. One has,

$$\mathbf{d}_i(k)\cdot\mathbf{d}_f(k) = \sin^2 k + \cos^2 k - (g_i + g_f)\cos k + g_i g_f = 0. \quad \text{(E4)}$$

The solution exists when

$$|\cos k| = \left|\frac{1 + g_i g_f}{g_i + g_f}\right| < 1. \quad \text{(E5)}$$

One can obtain $\text{sgn}[(1 - |g_i|)(1 - |g_f|)] = -1$, i.e., DQPT occurs if and only if the initial Hamiltonian and the final

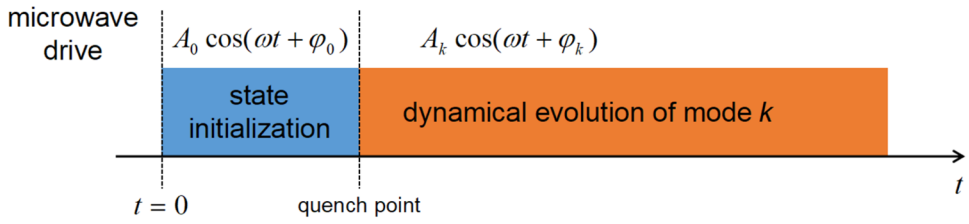

FIG. 6. Experiment control sequence. The initial state is prepared at the state-initialization period by control quantity $A_0\cos(\omega t+\varphi_0)$. The state is prepared as $|\phi_i\rangle$. Then for a quantum quench, by controlling φ_k depending on momentum k, we adjust the direction of the rotation axis, shown in Eq. (B7).

Hamiltonian belong to different phases for the Ising model, and $k^*=\pm\arccos[(1+g_ig_f)/(g_i+g_f)]$.

We also know from Refs. [24] and [26] that a dynamical Chern number can be defined in momentum-time space in a quench process. First we find the fixed points k_m that, satisfying $\hat{\mathbf{d}}_i(k_m)$, is parallel and antiparallel to $\hat{\mathbf{d}}_f(k_m)$. Here we just focus on the transverse-field Ising model, there are only two fixed points $k=0$ and $k=\pi$. Then the dynamical Chern number is defined as

$$C_{\rm dyn}=\frac{1}{4\pi}\int_0^{\pi}dk\int_0^{\pi}dt'(\hat{\mathbf{d}}\times\partial_{t'}\hat{\mathbf{d}})\cdot\partial_k\hat{\mathbf{d}}, \tag{E6}$$

where $t'=t/\mathbf{d}_f$ is the rescaled time.

For the fixed point $k=0$, we have $\hat{\mathbf{d}}(0)=[0,\mathrm{sgn}(g-1),0]$, and for the fixed point $k=\pi$, we have $\hat{\mathbf{d}}(\pi)=[0,\mathrm{sgn}(g+1),0]$. The dynamical Chern number is calculated,

$$C_{\rm dyn}=\frac{1}{2}(\cos\theta_{k=0}-\cos\theta_{k=\pi}), \tag{E7}$$

where θ_k is the induced angle between $\hat{\mathbf{d}}_i(k)$ and $\hat{\mathbf{d}}_f(k)$. In our experiment, we first choose $g_i=0.2$ and $g_f=1.5$, hence $\hat{\mathbf{d}}_i(0)\cdot\hat{\mathbf{d}}_f(0)=-1$ and $\hat{\mathbf{d}}_i(\pi)\cdot\hat{\mathbf{d}}_f(\pi)=1$, the dynamical Chern number is $C_{\rm dyn}=-1$. As a result, the Bloch sphere is fully covered as shown in Fig. 2(g) in the main text. From the continuity of the function $\hat{\mathbf{d}}_i(k)\cdot\hat{\mathbf{d}}_f(k)$, there must be a critical momentum k^* between 0 and π satisfying $\hat{\mathbf{d}}_i(k^*)\cdot\hat{\mathbf{d}}_f(k^*)=0$, so we can draw a conclusion that the nontrivial dynamical Chern number ensures the occurrence of DQPT.

We also choose $g_i=0.2$ and $g_f=0.5$, we have $\hat{\mathbf{d}}_i(0)\cdot\hat{\mathbf{d}}_f(0)=\hat{\mathbf{d}}_i(\pi)\cdot\hat{\mathbf{d}}_f(\pi)=1$, and hence the dynamical Chern number $C_{\rm dyn}=0$. In this case, the Bloch sphere is not fully covered as shown in Fig. 2(n) in the main text, and the DQPT would not occur.

The nontrivial dynamical Chern number indicates the emergence of the Skyrmion lattice in the momentum-time space. If $g_i=0.2$ and $g_f=1.5$, the dynamical Chern number is nontrivial, we consider the expectation value

$$\langle\hat{\mathbf{d}}(k,t)\rangle\equiv\langle\phi(k,t)|\hat{\mathbf{d}}\cdot\sigma|\phi(k,t)\rangle=-\hat{\mathbf{d}}(k,t)\cdot\hat{\mathbf{d}}_i(k). \tag{E8}$$

At $k=k^*$ and $t=t_c$, $\langle\hat{\mathbf{d}}(k,t)\rangle$ reaches the minimum -1 and $(k,t)=(k^*,t_c)$ is the center in the texture of pseudospin as shown in Fig. 4(c). It forms a lattice during the time evolution with the lattice spacing is just the period of DQPT $\pi/|\mathbf{d}_f(k)|$. In the case $g_i=0.2$ and $g_f=0.5$, the DQPT would not occur, the dynamical Chern number is trivial and Skyrmion lattices would not appear as shown in Fig. 4(d) in the main text.

APPENDIX F: ERROR BAR SHOWN IN THE FIGURES

The dynamical free energy can be expressed in terms of $\hat{\mathbf{d}}_i(k)$ and $\hat{\mathbf{d}}(k,t)$

$$f(t)=-\frac{1}{N}\sum_k\log\frac{1+\hat{\mathbf{d}}_i(k)\cdot\hat{\mathbf{d}}(k,t)}{2}. \tag{F1}$$

In our experimental setup, $\hat{\mathbf{d}}_i(k)$ is a fixed unit vector. To estimate the experimental error of $f(t)$, we need only to estimate the fluctuation of $\hat{\mathbf{d}}_i(k)$. Given a specific k, we obtain 70 state tomography data $\hat{\mathbf{d}}(k,t)$ corresponding to different time points on the evolution path on the Bloch sphere. Each of these tomography data $\hat{\mathbf{d}}(k,t)$ is an average of 5000 raw data. We estimate the fluctuation of $\hat{\mathbf{d}}(k,t)$ by estimating the fluctuation of the radius of the evolution path traced on the Bloch sphere. For each path, we choose three equally separated state points $\hat{\mathbf{d}}(k,t)$ and calculate the radius determined. Thus for k, we obtain 22 estimations of the evolution path. The magnitude $\|\Delta\hat{\mathbf{d}}(k)\|$ of the fluctuation of $\hat{\mathbf{d}}(k,t)$ is evaluated by the standard deviation of the 22 estimations of the radius. The error of the dynamical free energy is hence

$$\Delta f(t)=\frac{1}{N}\sum_k\frac{\left\|\Delta\hat{\mathbf{d}}(k)\right\|}{1+\hat{\mathbf{d}}_i(k)\cdot\hat{\mathbf{d}}(k,t)}. \tag{F2}$$

Those error bars are indicated in Figs. 3 and 4 in the main text.

[1] J. Zhang, P. W. Hess, A. Kyprianidis, P. Becker, A. Lee, J. Smith, G. Pagano, I. D. Potirniche, A. C. Potter, A. Vishwanath, N. Y. Yao, and C. Monroe, Observation of a discrete time crystal, Nature **543**, 217 (2017).

[2] S. Choi, J. Choi, R. Landig, G. Kucsko, H. Zhou, J. Isoya, F. Jelezko, S. Onoda, H. Sumiya, V. Khemani, C. Keyserlingk, N. Y. Yao, E. Demler, and M. D. Lukin, Observation of discrete time-crystalline order in a disordered dipolar many-body system, Nature **543**, 221 (2017).

[3] J. Zhang, G. Pagano, P. W. Hess, A. Kyprianidis, P. Becker, H. Kaplan, A. V. Gorshkov, Z.-X. Gong, and C. Monroe, Observation of a many-body dynamical phase transition with a 53-qubit quantum simulator, Nature **551**, 601 (2017).

[4] H. Bernie, S. Schwartz, A. Keesling, H. Levine, A. Omran, H. Pichler, S. Choi, A. S. Zibrov, M. Endres, M. Greiner, V. Vuletić, and M. D. Lukin, Probing many-body dynamics on a 51-atom quantum simulator, Nature **551**, 579 (2017).

[5] P. Jurcevic, H. Shen, P. Hauke, C. Maier, T. Brydges, C. Hempel, B. P. Lanyon, M. Heyl, R. Blatt, and C. F. Roos, Direct Observation of Dynamical Quantum Phase Transitions in an Interacting Many-body System, Phys. Rev. Lett. **119**, 080501 (2017).

[6] N. Fläschner, D. Vogel, M. Tarnowski, B. S. Rem, D. Lühmann, M. Heyl, J. C. Budich, L. Mathey, K. Sengstock, and C. Weitenberg, Observation of dynamical vortices after quenches in a system with topology, Nat. Phys. **14**, 265 (2018).

[7] M. Schreiber, S. S. Hodgman, P. Bordia, H. P. Lüschen, M. H. Fischer, R. Vosk, E. Altman, U. Schneider, and I. Bloch, Observation of many-body localization of interacting fermions in a quasirandom optical lattice, Science **349**, 842 (2015).

[8] G. A. Alvarez, D. Suter, and R. M. Kaiser, Localization-delocalization transition in the dynamics of dipolar-coupled nuclear spins, Science **349**, 846 (2015).

[9] J. Y. Choi, S. Hild, J. Zeiher, P. Schauß, A. Rubio-Abadal, T. Yefsah, V. Khemani, D. A. Huse, I. Bloch, and C. Gross, Exploring the many-body localization transition in two dimensions, Science **352**, 1547 (2016).

[10] J. Smith, P. Richerme, B. Neyenhuis, P. W. Hess, P. Hauke, M. Heyl, M. A. Huse, and C. Monroe, Many-body localization in a quantum simulator with programmable random disorder, Nat. Phys. **12**, 907 (2016).

[11] K. Xu, J. J. Chen, Y. Zeng, Y. R. Zhang, C. Song, W. Liu, Q. Guo, P. Zhang, D. Xu, H. Deng, K. Huang, H. Wang, X. B. Zhu, D. N. Zheng, and H. Fan, Emulating Many-body Localization with a Superconducting Quantum Processor, Phys. Rev. Lett. **120**, 050507 (2018).

[12] P. Roushan et al., Spectroscopic signatures of localization with interacting photons in superconducting qubits, Science **358**, 1175 (2017).

[13] X. S. Tan, D. W. Zhang, Q. Liu, G. M. Xue, H. F. Yu, Y. Q. Zhu, H. Yan, S. L. Zhu, and Y. Yu, Topological Maxwell Metal Bands in a Superconducting Qutrit, Phys. Rev. Lett. **120**, 130503 (2018).

[14] X. S. Tan, M. M. Li, D. Y. Li, K. Z. Dai, H. F. Yu, and Y. Yu, Demonstration of Hopf-link semimetal bands with superconducting circuits, App. Phys. Lett. **112**, 172601 (2018).

[15] X. Y. Guo, Y. Peng, C. N. Peng, H. Deng, Y. R. Jin, C. Tang, X. B. Zhu, D. Zheng, and H. Fan, Demonstration of irreversibility and dissipation relation of thermodynamics with a superconducting qubit, arXiv:1710.10234.

[16] X. H. Peng, H. Zhou, B. B. Wei, J. Cui, J. F. Du, and R. B. Liu, Experimental Observation of Lee-Yang Zeros, Phys. Rev. Lett. **114**, 010601 (2015).

[17] C. Y. Lu, W. B. Gao, O. Gühne, X. Q. Zhou, Z. B. Chen, and J. W. Pan, Demonstrating Anyonic Fractional Statistics with a Six-qubit Quantum Simulator, Phys. Rev. Lett. **102**, 030502 (2009).

[18] Y. P. Zhong, D. Xu, P. Wang, C. Song, Q. J. Guo, W. X. Liu, K. Xu, B. X. Xia, C. Y. Lu, S. Han, J. W. Pan, and H. Wang, Emulating Anyonic Fractional Statistical Behavior in a Superconducting Quantum Circuit, Phys. Rev. Lett. **117**, 110501 (2016).

[19] E. A. Martinez, C. A. Muschik, P. Schindler, D. Nigg, A. Erhard, M. Heyl, P. Hauke, M. Dalmonte, T. Monz, P. Zoller, and R. Blatt, Real-time dynamics of lattice gauge theories with a few-qubit quantum computer, Nature **534**, 516 (2016).

[20] M. Heyl, A. Polkovnikov, and S. Kehrein, Dynamical Quantum Phase Transitions in the Transverse-field Ising Model, Phys. Rev. Lett. **110**, 135704 (2013).

[21] M. Heyl, Dynamical Quantum Phase Transitions in Systems with Broken-symmetry Phases, Phys. Rev. Lett. **113**, 205701 (2014).

[22] M. Heyl, Scaling and Universality at Dynamical Quantum Phase Transitions, Phys. Rev. Lett. **115**, 140602 (2015).

[23] J. Eisert, M. Friesdorf, and C. Gogolin, Quantum many-body systems out of equilibrium, Nat. Phys. **11**, 124 (2015).

[24] C. Yang, L. Li, and S. Chen, Dynamical topological invariant after a quantum quench, Phys. Rev. B **97**, 060304(R) (2018).

[25] H. F. Lang, Y. X. Chen, Q. T. Hong, and H. Fan, Dynamical quantum phase transition for mixed states in open systems, Phys. Rev. B **98**, 134310 (2018).

[26] Z. Gong and M. Ueda, Topological Entanglement-Spectrum Crossing in Quench Dynamics, Phys. Rev. Lett. **121**, 250601 (2018).

[27] E. Canovi, P. Werner, and M. Eckstein, First-order Dynamical Phase Transitions, Phys. Rev. Lett. **113**, 265702 (2014).

[28] J. C. Budich and M. Heyl, Dynamical topological order parameters far from equilibrium, Phys. Rev. B **93**, 085416 (2016).

[29] S. Sharma, U. Divakaran, A. Polkovnikov, and A. Dutta, Slow quenches in a quantum Ising chain: Dynamical phase transitions and topology, Phys. Rev. B **93**, 144306 (2016).

[30] Z. Huang and A. V. Balatsky, Dynamical Quantum Phase Transitions: Role of Topological Nodes in Wave Function Overlaps, Phys. Rev. Lett. **117**, 086802 (2016).

[31] T. Nemoto, R. L. Jack, and V. Lecomte, Finite-size Scaling of a First-order Dynamical Phase Transition: Adaptive Population Dynamics and an Effective Model, Phys. Rev. Lett. **118**, 115702 (2017).

[32] M. Heyl and J. C. Budich, Dynamical Topological Quantum Phase Transitions for Mixed States, Phys. Rev. B **96**, 180304(R) (2017).

[33] C. Yang, Y. Wang, P. Wang, X. Gao, and S. Chen, Dynamical Signature of Localization-delocalization Transition in a One-dimensional Incommensurate Lattice, Phys. Rev. B **95**, 184201 (2017).
[34] L. Zhou, Q. Wang, H. Wang, and J. Gong, Dynamical quantum phase transitions in non-Hermitian lattices, arXiv:1711.10741.
[35] M. Heyl, Dynamical quantum phase transitions: A review, Rep. Prog. Phys. **81**, 054001 (2018).
[36] A. A. Zvyagin, Dynamical quantum phase transitions, Low Temp. Phys. **42**, 971 (2016).
[37] R. Barends, J. Kelly, A. Megrant, D. Sank, E. Jeffrey, Y. Chen, Y. Yin, B. Chiaro, J. Mutus, C. Neill, P. O'Malley, P. Roushan, J. Wenner, T. C. White, A. N. Cleland, and J. M. Martinis, Coherent Josephson Qubit Suitable for Scalable Quantum Integrated Circuits, Phys. Rev. Lett. **111**, 080502 (2013).
[38] J. Koch, T. M. Yu, J. Gambetta, A. A. Houck, D. I. Schuster, J. Majer, A. Blais, M. H. Devoret, S. M. Girvin, and R. J. Schoelkopf, Charge-insensitive qubit design derived from the Cooper pair box, Phys. Rev. A **76**, 042319 (2007).
[39] R. Barends et al., Superconducting quantum circuits at the surface code threshold for fault tolerance, Nature **508**, 500 (2014).
[40] N. Ofek, A. Petrenko, R. Heeres, P. Reinhold, Z. Leghtas, B. Vlastakis, Y. Liu, L. Frunzio, S. M. Girvin, L. Jiang, M. Mirrahimi, M. H. Devoret, and R. J. Schoelkopf, Extending the lifetime of a quantum bit with error correction in superconducting circuits, Nature **536**, 441 (2016).
[41] A. Blais, R.-S. Huang, A. Wallraff, S. M. Girvin, and R. J. Schoelkopf, Cavity quantum electrodynamics for superconducting electrical circuits: An architecture for quantum computation, Phys. Rev. A **69**, 062320 (2004).
[42] W. Y. Su, J. R. Schrieffer, and A. J. Heeger, Solitons in Polyacetylene, Phys. Rev. Lett. **42**, 1698 (1979).
[43] A. Yu. Kitaev, Unpaired Majorana fermions in quantum wires, Phys. Usp. **44**, 131 (2001).
[44] E. Barouch and B. M. Mccoy, Statistical mechanics of XY-model. II. Spin-correlation functions, Phys. Rev. A **3**, 786 (1971).
[45] I. Martin, G. Refael, and B. Halperin, Topological Frequency Conversion in Strongly Driven Quantum Systems, Phys. Rev. X **7**, 041008 (2017).
[46] J. M. Fink, PhD thesis, ETH Zurich, 2010.
[47] S. M. Girvin, Circuit QED: Superconducting Qubits Coupled to Microwave Photons, Lecture Notes of the Les Houches Summer School 96 Chap. 3, 113–255 (Oxford University Press, 2011).
[48] G. Wendin, Quantum information processing with superconducting circuits: A review, Rep. Prog. Phys. **80**, 106001 (2017).
[49] X. Gu, A. F. Kockum, A. Miranowicz, Y. X. Liu, and F. Nori, Microwave photonics with superconducting quantum circuits, Phys. Rep. **718-719**, 1 (2017).
[50] S. Vajna and B. Dóra, Topological classification of dynamical phase transitions, Phys. Rev. B **91**, 155127 (2015).